Insight into the Effect of Oxygen Vacancy Concentration on the Catalytic Performance of MnO$_2$

Li Li,[†] Xianghong Feng,[†] Yao Nie,[†] Siguo Chen,[†] Feng Shi,[†] Kun Xiong,[†] Wei Ding,[†] Xueqiang Qi,[†] Jinsong Hu,[‡] Zidong Wei,*,[†] Li-Jun Wan,*,[‡] and Meirong Xia[†]

[†]State Key Laboratory of Power Transmission Equipment & System Security and New Technology, College of Chemistry and Chemical Engineering, Chongqing University, Chongqing 400044, China

[‡]Key Laboratory of Molecular Nanostructure and Nanotechnology, Institute of Chemistry, Chinese Academy of Sciences, Beijing 100190, China

S Supporting Information

ABSTRACT: Oxygen vacancies (OVs) are important for changing the geometric and electronic structures as well as the chemical properties of MnO$_2$. In this study, we performed a DFT+U calculation on the electronic structure and catalytic performance of a β-MnO$_2$ catalyst for the oxygen reduction reaction (ORR) with different numbers and extents of OVs. Comparing those results with the experimental XRD analysis, we determined that OVs produce a new crystalline phase of β-MnO$_2$. Changes in the electronic structure (Bader charges, band structure, partial density of states, local density of states, and frontier molecular orbital), proton insertion, and oxygen adsorption in β-MnO$_2$ (110) were investigated as a function

of the bulk OVs. The results show that a moderate concentration of bulk OVs reduced the band gap, increased the Fermi and HOMO levels of the MnO$_2$ (or MnOOH), and elongated the O−O bond of the adsorbed O$_2$ and coadsorbed O$_2$ with H. These changes substantially increase the conductivity of MnO$_2$ for the catalysis of ORR. However, an excessively high concentration of OVs in β-MnO$_2$ (110) will work against the catalytic enhancement of MnO$_2$ for ORR. The DFT+U calculation reveals that a moderate concentration of OVs induced a large overlap of the surface Mn d$_{z2}$ orbitals, thus introducing an extra donor level at the bottom of the conductive band, which increased the conductivity of β-MnO$_2$ (110). Such a curvilinear change of the catalytic activity and electronic structure as a function of the oxygen vacancy concentration suggests that the β-MnO$_2$ with moderate concentration OVs exhibits the highest conductivity and catalytic activity for ORR.

KEYWORDS: oxygen vacancy, oxygen reduction reaction, DFT, β-MnO$_2$, catalytic activity
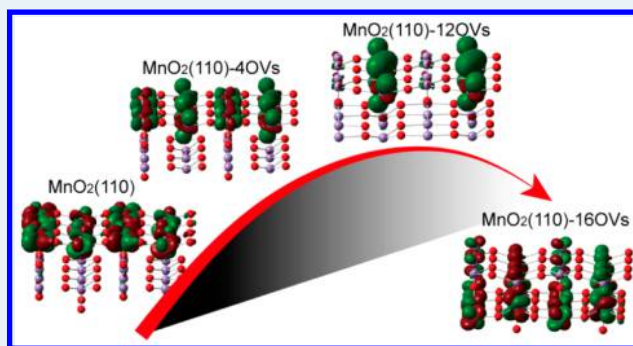
1. INTRODUCTION

The oxygen reduction reaction (ORR) is of prime importance in view of its practical applications in green energy conversion/storage systems ranging from fuel cells to metal/air batteries.[1,2] So far, noble metal catalysts, such as platinum, have played a dominant role in catalyzing the ORR,[3] but the high costs and limited availability of the requisite raw materials have seriously retarded large-scale commercial applications. This has led to an urgent need to explore inexpensive and abundant alternatives with a high activity that is comparable to precious-metal-based catalysts.

Among the nonprecious metal catalysts used for ORR, manganese oxides, as a very promising catalyst for the ORR in alkaline electrolytes, have attracted a substantial amount of attention because of their abundance, low-cost, and acceptable catalytic activity.[4−7] Jin et al.[8] reported that Ti-containing γ-MnO$_2$ hollow spheres exhibit a high specific capacity (2.2 Ah g^{-1} of carbon) in Li/air battery tests. Lee[9] developed a Zn−air battery based on α-MnO$_x$ nanowires in a Ketjenblack carbon air

cathode, which exhibits a peak power density of ∼190 mW/cm^2. In addition, manganese oxides can also be used in Li ion batteries,[6,10] supercapacitors,[11] and the catalytic oxygen evolution reaction (OER).[12]

The catalytic activity of transitional metal oxide nanoparticles can be improved through doping with cations, modulating the morphology and the crystal phase, coating with metals, and integrating conductive nanostructures.[7,13−22] For example, MnO$_x$ particles doped with transition metal (Pd, Au, Ag, Ni, Co, et al.) exhibited ORR-specific activities closed to the benchmark Pt/C catalyst.[15−20] Among MnO$_2$ phases, Cao ascertained that the catalytic activity sequence follows β- < λ- < γ- < α-MnO$_2$.[23] Being different from Cao's viewpoint, Cheng found that the catalytic activities follows another order of α- > β- > γ-MnO$_2$.[24] Xiao synthesized three types of MnO$_2$ nanostructures

and found that α-MnO_2 nanorods/tubes possess largely enhanced electrocatalytic activity compared with birnessite-type MnO_2 core—corona spheres.[25] Mao reported that the catalytic activity of manganese oxides toward ORR increased as follows: $Mn_5O_8 < Mn_3O_4 < Mn_2O_3 < MnOOH$.[26] Cheng et al.[27] found that the Mn_2O_3 nanowires that possessed a large aspect ratio and preferentially exposed (222) crystal facets exhibited significant activity toward ORR in alkaline solution.

In addition to the above approaches, introducing oxygen vacancies (OVs) is a relatively simple and economic alternative for developing high-performing electrocatalysts.[28−30] Depending on the sample treatment, thermal heating or radiation, OVs can be created in the bulk of and at the surface of metal oxides.[31−35] Kong[34] and Yan[35] et al. reported that tuning the relative concentration ratio of bulk OVs to surface OVs in TiO_2 can enhance the photocatalytic efficiency. Recently, the effect of OVs on the structure and catalytic activity of β-MnO_2 was investigated.[6,7,11,36,37] Cheng et al.[7] determined that the presence of OVs in β-MnO_2 enhances its catalytic activity in ORR. DFT calculations[7] were performed on β-MnO_2 (110) perfect surfaces and surfaces with one and two OVs, and the results showed that OVs reduce the kinetic barrier of the ORR. David A. Tompsett[6] et al. calculated the energetics of dilute oxygen vacancy formation at the β-MnO_2 surface and validated that OVs play an important role in improving the catalytic activity of β-MnO_2. These findings leave us with other questions: whether a higher oxygen vacancy concentration always leads to a higher ORR activity of MnO_2 and whether the bulk OVs play the same role as the surface OVs in enhancing the performance of MnO_2. In addition, the surface OVs on the β-MnO_2 is not stable and may disappear with the process of the ORR, which releases active O atoms. The released O atoms may fill in the surface oxygen vacancies. Therefore, the investigation of β-MnO_2 with the bulk OVs is more significant.

The mechanism of ORR catalyzed by MnO_2 has been extensively studied. It was proposed that a MnO_2-catalyzed ORR proceeds via 2-electron processes with hydrogen peroxide as an intermediate at low cathodic overpotentials,[23,38−42] and via a 4-electron process at high cathodic overpotentials, including a negligible hydrogen peroxide yield at high ORR overpotentials.[43] Because MnO_2 exhibits excellent activity for a HO_2^- disproportionation reaction into O_2 and OH^-,[42−47] the adsorption and dissociation of O_2 before the disproportion of HO_2^- plays an essential role in the ORR process.

In this paper, we apply first-principle simulations to understand the electronic and structural properties of β-MnO_2 in the presence of OVs in the bulk crystal and on subsurface sites, focusing on how the crystalline phase, conductivity, proton insertion process, and the catalytic activity of β-MnO_2 change with the presence of OVs. First, we calculate the XRD spectra of the model β-MnO_2 crystals, which are modulated with different oxygen vacancy concentrations. We then compare the experimental XRD results of the β-MnO_2 samples and the calculated XRD pattern of the model β-MnO_2 crystals to explore the correlation between the crystalline phase and the OVs. Second, the stable β-MnO_2 (110) is chosen to assess the effect of different numbers of subsurface and bulk OVs on the structure, conductivity, and catalytic activity of β-MnO_2. Meanwhile, we also investigate the influence of the presence of OV on the capacitive insertion of protons in the MnO_2 lattice and further bridge that to the ORR activity. Finally, the relationship between the electronic structure and the catalytic activity as a function of the oxygen vacancy concentration is determined.

2. EXPERIMENTAL AND COMPUTATIONAL DETAILS

2.1. Experimental Details. In a typical synthesis of β-MnO_2, a solution of reagent grade $Mn(NO_3)_2$ was dried, ground, and calcinated at 270, 340, and 450 °C, respectively, in an O_2 atmosphere.[48] The phase structure of the as-prepared samples was characterized using powder X-ray diffraction (XRD, Rigaku D/max-2500 diffractometer with Cu Kα radiation) and transmission electron microscopy (TEM, Zeiss LIBRA 200 TETEM, 200 kV). The electrochemical measurements were performed in a standard three-electrode cell at room temperature. The cell consisted of a glassy carbon working electrode (GC electrode, 3 mm in diameter), which is catalyzed by applying MnO_2 catalyst ink onto glassy carbon (GC) disk electrodes, a Ag/AgCl (3 M KCl) reference electrode, and a platinum foil counterelectrode. Briefly, the MnO_2 catalyst ink was prepared by mixing MnO_2 powders with carbon powders (Carbot, Vulcan-XC72) at a weight ratio of 20:80 in ethanol and ultrasonicated for 10 min. A total of 5 μL of well-dispersed catalyst ink was then applied to a prepolished GC disk. After drying at room temperature, a drop of 0.05 wt % Nafion solution was applied to the surface of the catalyst layer to form a thin catalyst film. For comparison, carbon powder without MnO_2 powders was also applied to the GC electrodes through the same procedures. The cyclic voltammetry (CV) curves were performed at potentials between 0 and 1.0 V versus a reversible hydrogen electrode (RHE) at a scan rate of 50 mV·s^{-1} in N_2 or O_2-purged 0.1 M KOH at room temperature (Figure s1). The RDE polarization curves (Figure s1) were tested using an O_2 or N_2 saturated 0.1 M KOH solution at 1600 rpm with a scan rate of 10 mV·s^{-1}. The CV accelerated stress tests (ASTs, listed in Figure s1) were performed at potentials between 0 and 1.2 V versus RHE at a scan rate of 50 mV·s^{-1} in N_2-purged 0.1 M KOH solutions at room temperature. Electrochemical tests were carried out at room temperature on a computer-controlled workstation (AutoLab).

2.2. Model and Computation Details. In this work, periodic density functional theory (DFT) calculations were carried out using the Perdew−Burke−Ernzerhof functional and projected augmented wave pseudopotentials, as embedded in the Vienna ab initio simulation package. The cutoff energy for the plane-wave basis set was verified by convergence testing. As shown in Figure 1a, the lattice parameters and energy of β-MnO_2 exhibit only a little change when the cutoff changes from 380 to 550 eV. Thus, considering the CPU time and the accuracy of the lattice parameters, the cutoff of 380 eV was selected to calculate the geometry and electronic structure of β-MnO_2. For the β-MnO_2 structures, DFT+U calculations[36,49] with an empirical Coulomb term U value of 4 eV and without the exchange term J value is employed to model the orbital-dependent Hubbard-like potential for the Mn d states. The effect of the exchange term J value on the results of the calculation was tested by comparing the change in the filled density of state (DOS) of β-MnO_2 (110), which is the focus of this work. As shown in Figure 1b, the DOSs of β-MnO_2 (110) coincide with each other in the filled DOS, regardless if the J value is 1.2 or 0 eV. Thus, the J value is not necessary for accurate results in the this work.

XRD of the β-MnO_2 crystal with OVs was simulated by the Reflex software package from material studio (MS) using 48-atom $2 \times 2 \times 2$ supercells ($Mn_{16}O_{32}$) with periodic boundary conditions. As shown in Figure 2a, models of $Mn_{16}O_{32}$ with 2, 4, 6, and 8 OVs are constructed, forming 1/16, 1/8, 3/16 and 1/4 oxygen vacancy concentrations, respectively. Considering the symmetry, the OVs in the models were distributed evenly. The
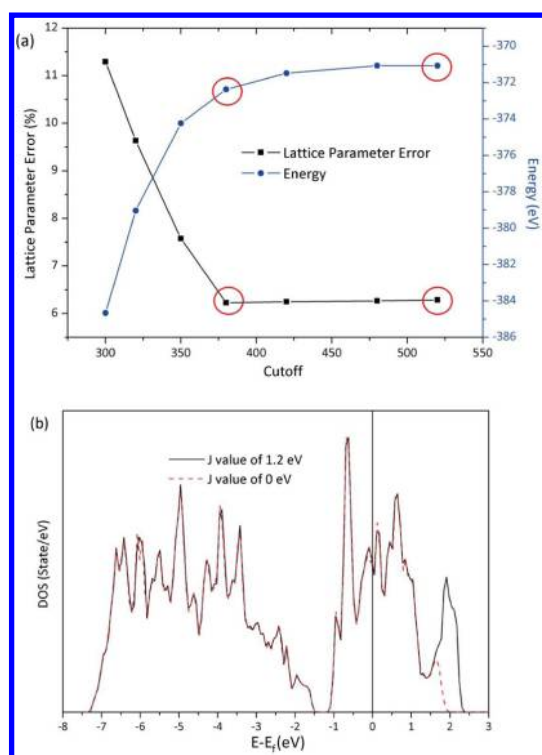
Figure 1. (a) Effect of the cutoff on the energy and lattice parameter error of β-MnO$_2$ crystal and (b) the comparison of the DOS calculated using a J value of 1.2 and 0 eV for the perfect β-MnO$_2$ (111).
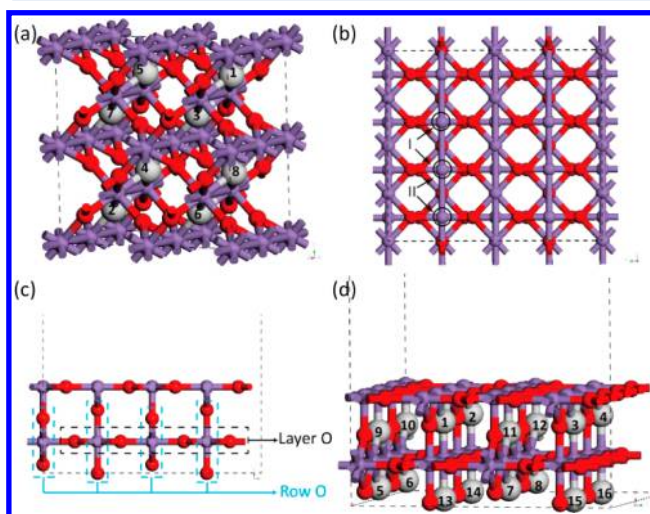

Figure 2. (a) β-MnO$_2$ (2 × 2 × 2) supercell model with a different number of OVs; (b) the top plane view of β-MnO$_2$ (110), where I and II are the oxygen adsorption sites; (c) the types of O atoms in β-MnO$_2$ (110); and (d) the side views of β-MnO$_2$ (110) with different numbers of OVs. Purple balls represent the Mn atoms, red balls represent the O atoms, and gray balls represent the OVs.

lattice parameters and all the atomic positions were allowed to relax until the forces on the atoms were <0.0001 eV/Å. For the Brillouin zone integration, a 3 × 3 × 3 Monkhorst−Pack k-point mesh was used. The MnO$_2$ crystallized in a rutile structure with a $P4/mnm$ space group, in which each Mn atom was 6-fold-coordinated with oxygen and each O atom was 3-fold-coordinated with the Mn. The calculated equilibrium lattice parameters, a = 4.40 and c = 2.71, are very close to the experimental values (a = 4.398 and c = 2.873).

The most stable and active low-index surface,[10,37,50] β-MnO$_2$ (110), was chosen for the investigation of the influence of OVs on the catalytic activity of β-MnO$_2$. TEM characterizations (Figure s2) of β-MnO$_2$ verifies that the MnO$_2$ (110) is one of the preferentially exposed surfaces. To match the stoichiometry of MnO$_2$ crystal, as shown in Figure 2b, the top of the MnO$_2$ (110) slab was terminated by a Mn−O layer, and the bottom was terminated by an O layer. The dipole correction was used to investigate the effect of the unrealistic dipole momentum of the nonsymmetric β-MnO$_2$ (110) slab. Figure s3 shows that the DOSs of β-MnO$_2$ (110) coincide with each other in the filled orbital states before and after dipole correction, and the effect of the unrealistic dipole momentum on the electronic structure of β-MnO$_2$ (110) can be omitted.

To ensure that the number of atoms on the surface of stoichiometric and nonstoichiometric β-MnO$_2$ (110) was the same, the subsurface and bulk OVs were used. Two types of OVs were considered, including row OVs and layer OVs, by removing different types of O atoms (row and layer O shown in Figure 2c). A structure calculation (Figure s4) illustrates that the MnO$_2$ with layer OVs obviously deforms and is more unstable, with an increase in the OVs. Then, in this work, defective β-MnO$_2$ (110) with OVs was modeled by removing 4, 8, 12, and 16 row O atoms from the 4 × 2 × 2 slab (Mn$_{32}$O$_{64}$) subsurface, respectively, producing 1/16, 1/8, 3/16, and 1/4 oxygen vacancy concentrations, respectively. Figure 2d shows the position of the row OVs in β-MnO$_2$ (110). Over the surface, a vacuum space of 15 Å was set between two neighboring images, and all the atom positions were relaxed until the atomic forces were reduced to <0.01 eV/ Å. For the Brillouin zone integration, a 3 × 3 × 1 Monkhorst−Pack k-point mesh was used, and a more refined 9 × 9 × 1 k-point mesh was used for the DOS and band structure plots.

To understand the catalytic activity of β-MnO$_2$ for the ORR, the oxygen adsorption of β-MnO$_2$ (110) was calculated via bridge type. As shown in Figure 2b, there are two bridge adsorption sites. For perfect β-MnO$_2$ (110), site I is equal to site II. For defective β-MnO$_2$ (110) with OVs, site I differs from site II because the OVs induced a distortion of the structure of the β-MnO$_2$ (110). The high concentration of OVs (16 OVs) results in the closeness of the Mn atoms at site II, whereas other OV contents induce the nearness of the Mn atoms at site I.

3. RESULTS AND DISCUSSION

3.1. ORR Activity and XRD of β-MnO$_2$ Catalysts. The polarization curves for the electrodes catalyzed by carbon— MnO$_2$/C (270 °C), MnO$_2$/C (340 °C), and MnO$_2$/C (450 °C)—in an O$_2$-saturated 0.1 M aqueous KOH solution using a rotating disk electrode (RDE) at 1600 rpm are shown in Figure 3. MnO$_2$ (340 °C)/C exhibits the best ORR catalytic performance among all the studied catalysts in terms of the overpotential, onset ORR potential, and the ORR current. The catalytic activity for the ORR follows the order MnO$_2$/C (340 °C) > MnO$_2$/C (270 °C) > MnO$_2$/C (450 °C).

To search for the structure−activity relationship of MnO$_2$, we have performed a structural characterization. From the experimental XRD spectra in Figure 4a, MnO$_2$ catalysts obtained at different temperatures exhibit a similar average particle size of ∼25 nm (Table s1) and a similar stable crystal structure. As shown in Figure 4a, the MnO$_2$ obtained at 450 °C is determined to be a pure tetragonal phase of β-MnO$_2$ (JCPDS no. 624-0735) with lattice constants of a = 4.399 Å and c = 2.874 Å. When the pyrolysis temperature decreases to 340 and 270 °C, the main
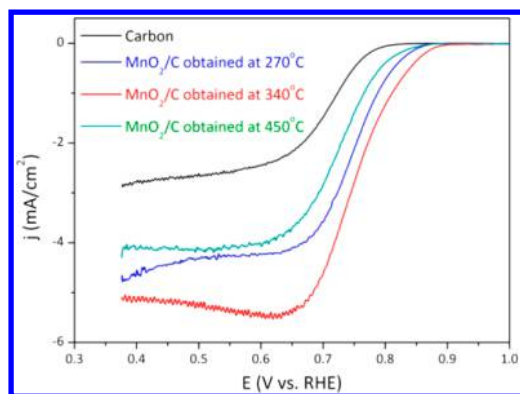
Figure 3. ORR polarization curves of electrodes made from carbon and MnO_2/C obtained at 270, 340, and 450 °C in an O_2-saturated 0.1 M KOH solution at room temperature (1600 rpm, sweep rate 10 mV·s^{-1}).
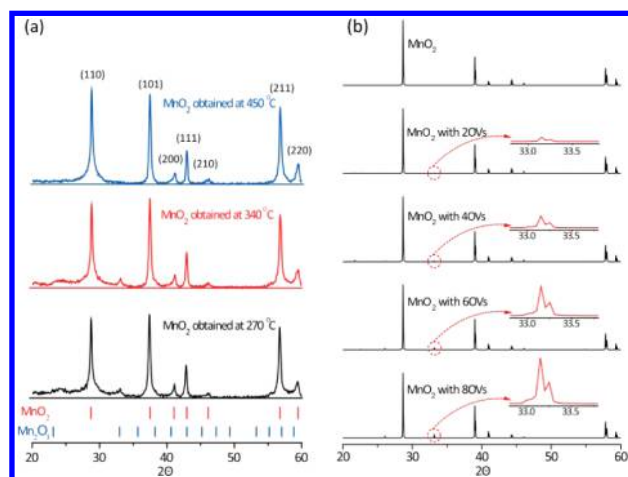

Figure 4. (a) Experimental XRD spectra of MnO_2 and (b) simulated XRD spectra of β-MnO_2 crystals with different numbers of OVs. (MnO_2 JCPDS 24-0735; Mn_2O_3 JCPDS 41-1441).

diffraction peaks still correspond to a tetragonal phase of β-MnO_2, except for the generation of a new diffraction peak at $2\theta = 33.2°$ ($d = 2.72$ Å). Thus, the enhanced catalysis of MnO_2 obtained at 340 and 270 °C relative to that at 450 °C might be ascribed to the formation of a new crystalline phase with a d value of 2.72 Å. Although the peak at 33.2° is a characteristic peak of Mn_2O_3 (JCPDS no. 41-1441), other characteristic peaks of Mn_2O_3 do not emerge. In addition, the pyrolysis temperatures of 270 or 340 °C are too low to produce Mn_2O_3. Therefore, the peak of the XRD spectra at 33.2° might be a result of the low-oxidation-state Mn cation for the inadequate pyrolysis of $Mn(NO_3)_2$ in O_2 at a relatively low temperature.[51]

It is well-known that OVs give rise to a change in cation valence states. At very high oxygen vacancy concentrations, oxides can be reduced to form a new stable phase that contains only low-oxidation-state cations.[52] Thus, we simulated the XRD of β-MnO_2 crystals with different numbers of OVs to reveal the new crystalline structure at 33.2° in the XRD spectra of β-MnO_2. As shown in Figure 4b, there is a new peak at 33.2° in the simulated XRD spectra of the β-MnO_2 crystal with more or less OVs and in the experimental XRD spectra of β-MnO_2. This means that the OVs lead to the diffraction peak at 33.2° in the XRD spectra of β-MnO_2. Accordingly, the enhanced catalysis of MnO_2 obtained at 340 °C is intimately associated with the presence of OVs. Interestingly, the intensity of the peak at 33.2°

increases proportionally with increasing oxygen vacancy concentration. This phenomenon validates that the new XRD peak at 33.2° in β-MnO_2 pyrolyzed at 270 and 340 °C is attributed to the OVs or, in other words, the low-oxidation-state Mn cation. Thus, β-MnO_2 crystals with different numbers of OVs can simulate the structure of β-MnO_2 obtained at different temperatures.

On the basis of the relation between the crystalline phase and the OVs, as well as the similar particle size of as-prepared MnO_2 catalysts, the difference in the ORR catalytic activity of the MnO_2 obtained at different temperatures can be understood by exploring the difference in the electronic structure of β-MnO_2 with different oxygen vacancy concentrations.

3.2. Geometric and Electronic Structure of β-MnO_2 (110). To understand the effects of the oxygen vacancy concentration, the geometric and electronic structure of β-MnO_2 (110), including the Bader charges, band structure, partial density of states (PDOS), and the local density of states (LDOS), were calculated as a function of the oxygen vacancy concentration.

Figure 5 illustrates the stable geometric structure and band structure of β-MnO_2 (110) with different numbers of OVs. The stable geometric structure of MnO_2 (110) shows the stability of MnO_2 (110) with OVs. Compared with the stoichiometry MnO_2 (110), all defective MnO_2 (110) with OVs but 16 OVs shows slight bond contact between the surface layer atoms. The obvious structural distortion occurs only in the case of MnO_2 (110) with 16 OVs because too much oxygen is absent.

The band structure in Figure 5 determines that OVs have a significant effect on the conductivity of the MnO_2. As shown in Figure 5a, β-MnO_2 (110) is a transparent n-type semiconductor for the Fermi level lying next to the bottom of the conduction band (CB). The calculated band gap for perfect β-MnO_2 (110) is 0.267 eV, which is in good agreement with the previously reported[53] band gap of MnO_2 crystals. The calculated band structures of defective β-MnO_2 (110) with different numbers of OVs are shown in Figure 5b−e. For defective β-MnO_2 (110) with OVs, an extra band, marked in red, appears near the bottom of the CB, in contrast to the perfect β-MnO_2 (110). The extra donor level becomes increasingly more extensive until the number of OVs reaches 12. At the same time, the band gap of β-MnO_2 (110) becomes narrower until the number of OVs reaches 12 and subsequently suddenly becomes broad. The narrow band gap indicates a high conductivity. This suggests that a moderate oxygen vacancy concentration can effectively enhance the conductivity of the β-MnO_2, and an excessively high oxygen vacancy concentration is harmful to the enhancement of the conductivity of the MnO_2.

Although the conductivity of MnO_2 electrodes could be seemingly improved by mixing with Vulcan carbon powders, the performance for catalysis of the ORR is different from that of the specific MnO_2 samples, which was obtained at different pyrolysis temperatures. The addition of Vulcan carbon powders into the MnO_2 electrode solves the conductive problem between MnO_2 particles but does not solve the conductive problem of the MnO_2 particles themselves. It is from MnO_2 particles rather than from added carbon powders that O_2 molecules obtain electrons. Therefore, the good electric conductivity of MnO_2 particles themselves is critical for the ORR.

The PDOS of the β-MnO_2 (110) are presented in Figure 6. It shows that the extra donor level in the band structure of the defective β-MnO_2 (110) with OVs is mainly composed of Mn d orbitals. The bottom of the CB of the β-MnO_2 (110) is also

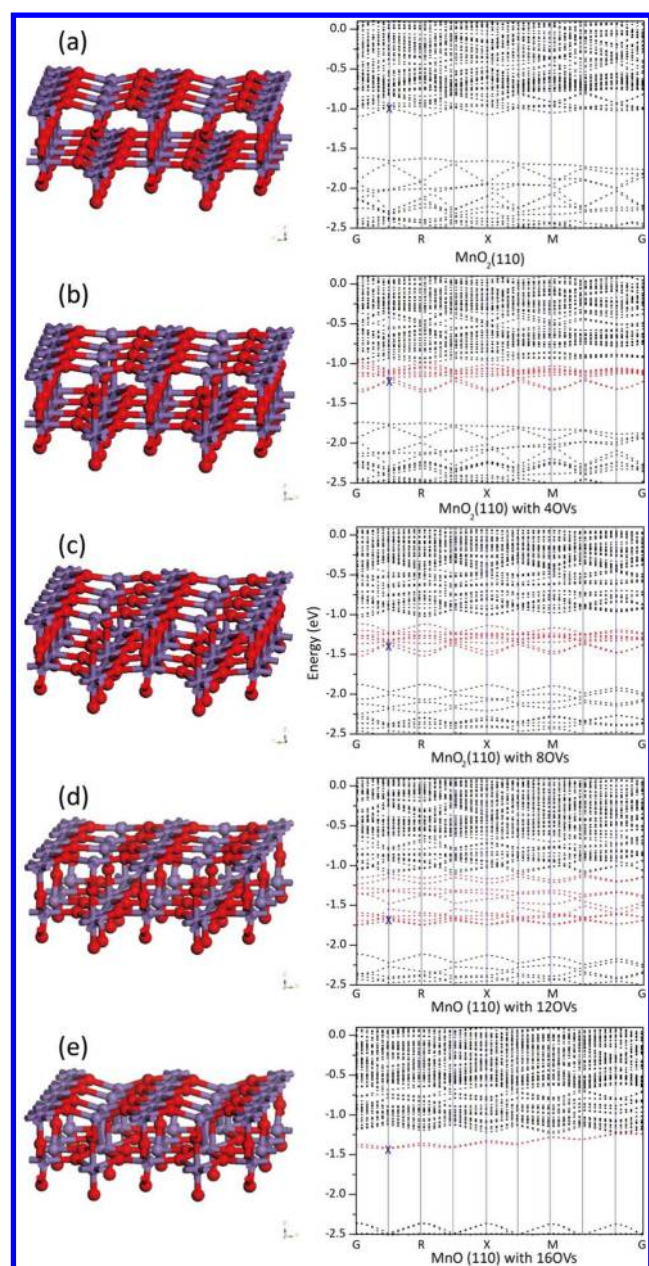**Figure 5.** (a) Geometric structure (left) and band structure (right) of β-MnO$_2$ (110), (b) MnO$_2$ (110) with 4 OVs, (c) MnO$_2$ (110) with 8 OVs, (d) MnO$_2$ (110) with 12 OVs, and (e) MnO$_2$ (110) with 16 OVs.

Figure 6. PDOS of β-MnO$_2$ (110) with OVs.

Figure 7. LDOS of β-MnO$_2$ (110) with OVs.

mainly attributed to the Mn d orbitals, and its upper VB is composed of O p and Mn d orbitals. Compared with the perfect β-MnO$_2$ (110), in the case of β-MnO$_2$ (110) with OVs, the numbers of Mn d orbitals at the bottom of the CB and the upper VB are increased. The increased Mn d orbital gradually broadens and shifts to the low-energy direction with increasing numbers of OVs, which results in a narrow band gap. However, as the number of OVs increases to 16, the number of Mn d orbitals at the bottom of the CB decreases sharply, and subsequently, the band gap is widened.

To further understand the effect of OVs on the PDOS and band structure of β-MnO$_2$ (110), we analyzed the LDOS at the bottom of the CB and the molecular orbital maps of the extra donor level (× point, shown in Figure 5) in the band structure. Figure 7 demonstrates that the bottom of the CB of the perfect β-MnO$_2$ (110) is mainly composed of the surface Mn atom d$_{x2−y2}$
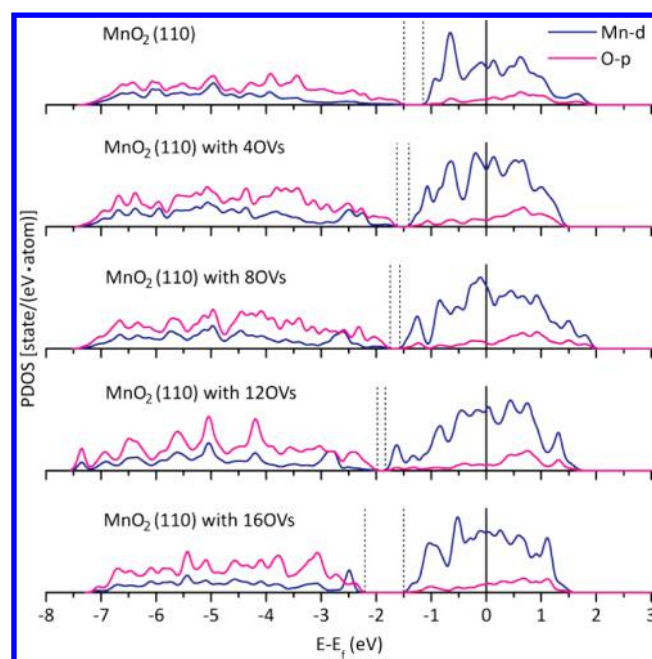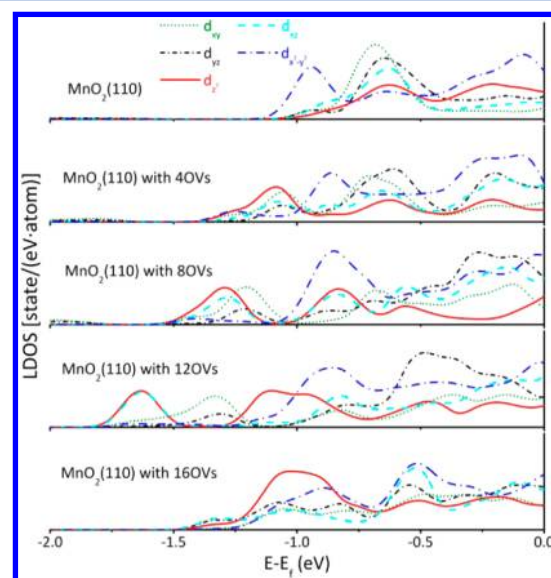
orbitals. In the case of OVs, the surface Mn d orbitals of the β-MnO$_2$ (110) have lower energies, except for the d$_{x2−y2}$ orbital. As the number of OVs increases, the surface Mn d$_{z2}$, d$_{xy}$, d$_{yz}$ and d$_{xz}$ orbitals move toward the low-energy direction; in particular, the Mn d$_{z2}$ shifts more noticeably. The lower-lying d$_{z2}$ orbitals are attributed to the large interaction between the surface Mn atoms around OVs. As shown in Figure 8, the overlap of the d$_{z2}$ orbitals of the surface Mn atoms around the OVs is continuously enlarged until the number of OVs increases to 12. As the number of OVs increases to 16, the interaction among the surface Mn atoms disappears, and subsequently, the lower-lying d orbitals fade away. This is followed by the band gap broadening. The phenomena indicate that structure distortion resulting from the presence of OVs and the electron transfer from the OVs to the surface Mn and O atoms causes the changes in the electronic structure of β-MnO$_2$ (110).
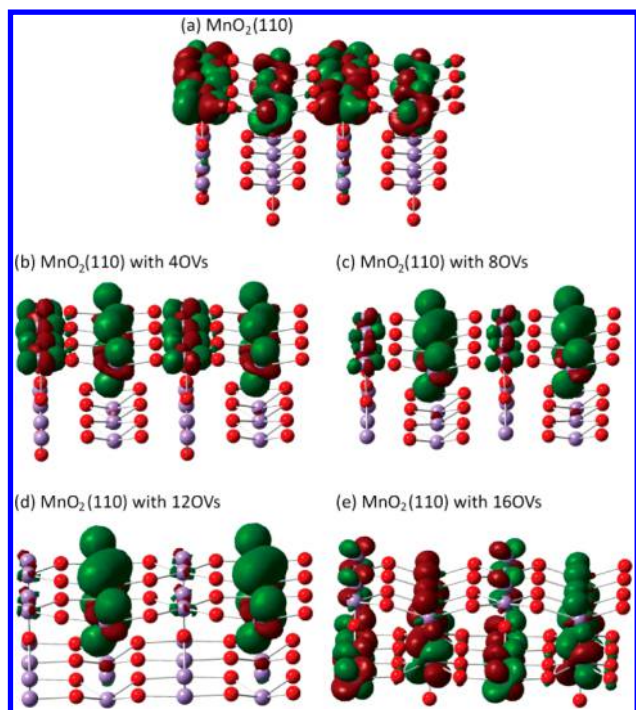
Figure 8. Molecular orbital maps of the extra donor level (× point in Figure 5) at the bottom of the CB.

Table 1 displays the average Bader charge of the β-MnO$_2$ (110). The Bader charges of the Mn and O atoms decrease with

Table 1. Average Bader Charge of β-MnO$_2$ (110) with OVs

av Bader charge	total Mn atoms	total O atoms	surface Mn atoms	surface O atoms
MnO$_2$ (110)	1.555	−0.778	1.463	−0.938
MnO$_2$ (110) with 4OVs	1.453	−0.775	1.333	−0.968
MnO$_2$ (110) with 8OVs	1.400	−0.800	1.285	−0.979
MnO$_2$ (110) with 12OVs	1.335	−0.821	1.232	−0.993
MnO$_2$ (110) with 16OVs	1.274	−0.850	1.213	−0.960

increasing numbers of OVs. Compared with the perfect β-MnO$_2$ (110), the defective β-MnO$_2$ (110) with OVs has a lower charge because of electron transfer from the OVs to the Mn and O atoms. The optimized stable structures of the β-MnO$_2$ (110) are shown in Figure 5. It is observed that the defective β-MnO$_2$ (110) with OVs has a shortened surface Mn−Mn bond compared with the perfect β-MnO$_2$ (110). The effect of the combination of the structure distortion and the average Bader charge on the MnO$_2$ (110) surface is embodied in the total charge density of the β-MnO$_2$ (110) with OVs. As shown in Figure 9, the total charge density between the surface Mn atoms around OVs (site I) increases until the number of OVs increases to 12. As the number of OVs increases to 16, the charge density between the Mn atoms is weakened. Meanwhile, the charge density between the Mn and O atoms is clearly enhanced.

3.3. The Catalytic Activity of β-MnO$_2$ (110) for ORR. It well-known that MnO$_2$ undergoes the reversible proton insertion process in the ORR potential range.[43,46]
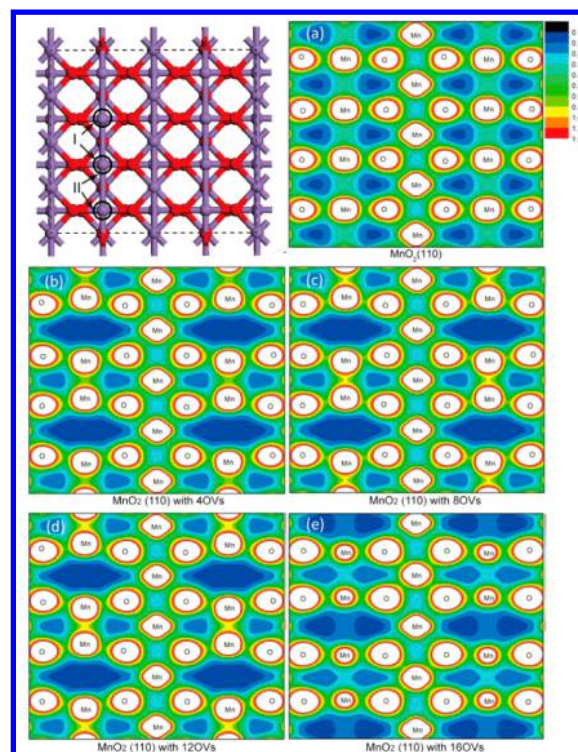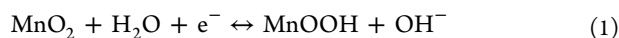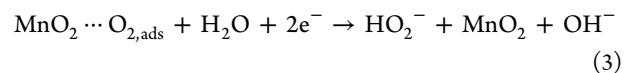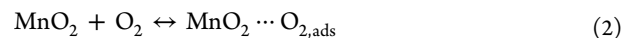
$$\text{MnO}_2 + \text{H}_2\text{O} + \text{e}^- \leftrightarrow \text{MnOOH} + \text{OH}^- \tag{1}$$

Figure 9. (a) Total charge density of β-MnO$_2$ (110), (b) MnO$_2$ (110) with 4 OVs, (c) MnO$_2$ (110) with 8 OVs, (d) MnO$_2$ (110) with 12 OVs, and (e) MnO$_2$ (110) with 16 OVs.

We then first investigated the effect of the OVs on the proton insertion (1) by calculating the H adsorption on the β-MnO$_2$ (110) as a function of the number of OVs (Figure s5). Compared with the perfect β-MnO$_2$ (110), the defective β-MnO$_2$ (110) has a relatively weak interaction with the H atom, except the β-MnO$_2$ (110) with 16 OVs. The difference in the H adsorption energy ($E_{\text{ads,H}}$) between the perfect and defective β-MnO$_2$ (110) is ~0.5 eV, which is roughly equivalent to the physical adsorption energy. The results mean that the OVs have trivial impact on the proton insertion process of MnO$_2$ compared with perfect MnO$_2$. The higher $E_{\text{ads,H}}$ on β-MnO$_2$ (110) with 16 OVs as an exception resulted mainly from the structural instability induced by the proton.

At low cathodic overpotentials, the ORR mechanism of OH$^-$ production on MnO$_2$ can be described by a partial reduction with 2 electrons, yielding hydrogen peroxide ions HO$_2^-$.[23,38−42,44]
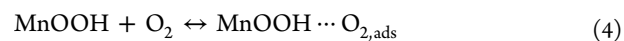
$$\text{MnO}_2 + \text{O}_2 \leftrightarrow \text{MnO}_2 \cdots \text{O}_{2,\text{ads}} \tag{2}$$

$$\text{MnO}_2 \cdots \text{O}_{2,\text{ads}} + \text{H}_2\text{O} + 2\text{e}^- \rightarrow \text{HO}_2^- + \text{MnO}_2 + \text{OH}^- \tag{3}$$

or

$$\text{MnOOH} + \text{O}_2 \leftrightarrow \text{MnOOH} \cdots \text{O}_{2,\text{ads}} \tag{4}$$

$$\text{MnOOH} \cdots \text{O}_{2,\text{ads}} + \text{e}^- \rightarrow \text{HO}_2^- + \text{MnO}_2 \tag{5}$$

Because MnO$_2$ exhibits excellent activity for a HO$_2^-$ disproponation reaction into O$_2$ and OH$^-$, the electron transfer from MnO$_2$ (or MnOOH) to O$_2$ and the activation of O$_2$ should be the vital steps for ORR to proceed smoothly on β-MnO$_2$.

The electron transfer capability of the β-MnO$_2$ catalyst can be acquired through matching the highest occupied molecular orbital (HOMO) level of catalysts with the lowest unoccupied

molecular orbital (LUMO) of O_2, and the symmetry, extent of overlap, and energy difference of these frontier orbitals dominate the extent of the interaction between the catalysts HOMO and the O_2 LUMO according to frontier molecular orbital theory. Then the larger the interaction between the HOMO and LUMO is, the easier and faster electron transfer is. As shown in Figure s6, the HOMO of β-MnO$_2$ (110) with different numbers of OVs is mainly composed of the Mn d orbital and has the same symmetry as the O_2 LUMO.[54] The HOMO of defective β-MnO$_2$ (110) has a larger spatial size than that of stoichiometric β-MnO$_2$ (110).

The relationship between the HOMO (or Fermi) level and the oxygen vacancy concentration is curvilinear listed in the Figure 10. It shows that the HOMO (Fermi) energy of β-MnO$_2$ (110)
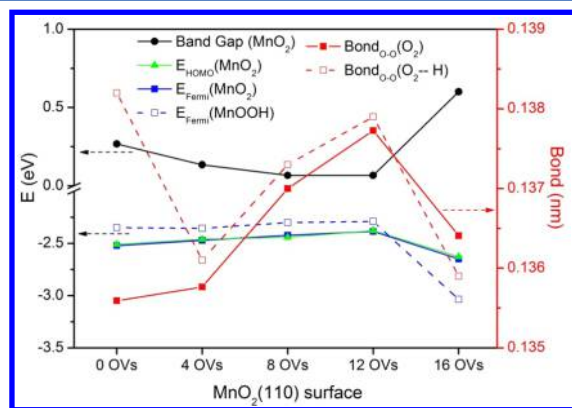

Figure 10. Changes in the band gap, E_{HOMO}, and E_{Fermi} of β-MnO$_2$, E_{Fermi} of MnOOH, and O−O bond as a function of the OV concentration.

continues to increase before the number of OVs increases to 12 and subsequently decreases suddenly. The HOMO (Fermi) of β-MnO$_2$ (110) with 16 OVs has the lowest energy, and the HOMO (Fermi) of β-MnO$_2$ (110) with 12 OVs has the highest energy. Similarly, after H adsorption, the Fermi level of MnOOH with OVs still has the same variation as that of MnO$_2$ with OVs. The tendency of the HOMO and Fermi level indicates that the moderate oxygen vacancy concentration benefits the electron transfer from the MnO$_2$ (or MnOOH) HOMO to O_2 LUMO.

The activation of O_2 is embodied by the length of the O−O bond in the solo adsorbed O_2 (Figure s7) and the coadsorbed O_2 with H (O_2−H) (Figure s8). As shown in Figure 10, the length of the O−O bond of the adsorbed O_2 increases before the number of OVs reaches 12 and subsequently decreases when the number of OVs reaches 16. Similarly, the O−O bond of the O_2−H on defective MnOOH follows the same tendency as that of solo O_2 adsorption on the β-MnO$_2$ with OVs. The noticeable activation of the O−O bond by the H is observed only on the perfect β-MnO$_2$ (110). The influence of the H in defective β-MnO$_2$ on the O−O bond activation and Fermi energy is limited, and usually, the defective β-MnO$_2$ is a more common state of β-MnO$_2$ relative to the perfect β-MnO$_2$. The elongated O−O bond reveals that the O−O bond can be more easily activated and dissociated; in other words, the β-MnO$_2$ (110) with 12 OVs benefits the activation and dissociation of O_2 easier.

Combining the electron transfer and the activation of the O−O bond, we can ascertain that β-MnO$_2$ (110) with 12 OVs is beneficial to the catalysis of ORR, but β-MnO$_2$ (110) with 16 OVs is bad for catalysis of ORR. β-MnO$_2$ (110) with 16 OVs has the stoichiometry of Mn$_2$O$_3$. According to our previous work, the catalytic activity of Mn$_2$O$_3$ is inferior to any MnO$_2$ catalysts

obtained from pyrolysis of Mn(NO$_3$)$_2$ at different temperatures, which is consistent with other published research.[26,55]

In summary, the HOMO, Fermi level and O−O bond vs the number of OVs follows the same tendency as the conductivity. The narrow band gap means a high electronic conductivity, which induces a lower electron transport resistance of the β-MnO$_2$ particles themselves and an easy electron transfer from MnO$_2$ particles to O_2 molecules. Therefore, the catalytic activity of β-MnO$_2$ is associated with the conductivity, HOMO, and Fermi level of β-MnO$_2$. The curvilinear change of the catalytic activity and electronic structure of β-MnO$_2$ as a function of the oxygen vacancy concentration suggests that the moderate oxygen vacancy concentration in defective β-MnO$_2$ would achieve the highest conductivity and catalytic activity.

4. CONCLUSION

In this work, we investigated the effect of the oxygen vacancy concentration on the crystalline phase, electronic structure, and catalytic activity of β-MnO$_2$ for ORR through a combination of experiments and DFT+U calculations. The comparison between the experimental XRD analysis of MnO$_2$ catalysts and the simulated XRD analysis of β-MnO$_2$ crystals validated the idea that OVs induce the formation of a new crystalline structure and change the catalytic activity of β-MnO$_2$. The changes of the electronic structure, proton insertion, and oxygen adsorption of β-MnO$_2$ (110) as a function of the oxygen vacancy concentration were investigated. The results indicate that moderate oxygen vacancy concentrations narrow the band gap, increase the HOMO and Fermi levels of β-MnO$_2$ (or MnOOH), and elongate the O−O bond of the adsorbed O_2 and coadsorbed O_2 and H. In addition, the OVs have a trivial impact on the proton insertion process of defective MnO$_2$. Such changes make MnO$_2$ very promising as a catalyst for ORR. However, an excessive concentration of OVs in β-MnO$_2$ (110) degrades the catalytic enhancement of MnO$_2$ for ORR. The modification of the electronic structure of defective β-MnO$_2$ (110) with OVs is attributed mainly to the structure distortion and the electron transfer from OVs to Mn and O atoms, which leads to a large overlap of the surface Mn d$_{z2}$ orbitals and subsequently introduces extra donor levels at the bottom of the CB. Therefore, the electronic structure and catalytic performance of β-MnO$_2$ can be effectively modulated by regulating the oxygen vacancy concentration.

■ ASSOCIATED CONTENT

ⓢ Supporting Information
The Supporting Information is available free of charge on the ACS Publications website at DOI: 10.1021/acscatal.5b00320.

> More details of characterization, electrochemical studies, and computational results (PDF)

■ AUTHOR INFORMATION

Corresponding Authors
*E-mail: zdwei@cqu.edu.cn.
*E-mail: wanlijun@iccas.ac.cn.
Notes
The authors declare no competing financial interests.

■ ACKNOWLEDGMENTS

■ REFERENCES

(1) Miyabayashi, K.; Nishihara, H.; Miyake, M. *Langmuir* **2014**, *30*, 2936−2942.

(2) Wei, W.; Liang, H.; Parvez, K.; Zhuang, X.; Feng, X.; Mullen, K. *Angew. Chem., Int. Ed.* **2014**, *53*, 1570−1574.

(3) Kim, T. J.; Kwon, G.; Kim, Y. T. *Chem. Commun. (Cambridge, U. K.)* **2014**, *50*, 596−598.

(4) Yang, Z.; Zhou, X.; Jin, Z.; Liu, Z.; Nie, H.; Chen, X.; Huang, S. *Adv. Mater.* **2014**, *26*, 3156−3161.

(5) Gnana Kumar, G.; Awan, Z.; Suk Nahm, K.; Xavier, J. S. *Biosens. Bioelectron.* **2014**, *53*, 528−534.

(6) Tompsett, D. A.; Parker, S. C.; Islam, M. S. *J. Am. Chem. Soc.* **2014**, *136*, 1418−1426.

(7) Cheng, F.; Zhang, T.; Zhang, Y.; Du, J.; Han, X.; Chen, J. *Angew. Chem., Int. Ed.* **2013**, *52*, 2474−2477.

(8) Jin, L.; Xu, L.; Morein, C.; Chen, C. H.; Lai, M.; Dharmarathna, S.; Dobley, A.; Suib, S. L. *Adv. Funct. Mater.* **2010**, *20*, 3373−3382.

(9) Lee, J.-S.; Park, G. S.; Lee, H. I.; Kim, S. T.; Cao, R.; liu, M. L.; Cho, J. *Nano Lett.* **2011**, *11*, 5362−5366.

(10) Mellan, T. A.; Maenetja, K. P.; Ngoepe, P. E.; Woodley, S. M.; Catlow, C. R. A.; Grau-Crespo, R. *J. Mater. Chem. A* **2013**, *1*, 14879−14887.

(11) Tompsett, D. A.; Parker, S. C.; Bruce, P. G.; Islam, M. S. *Chem. Mater.* **2013**, *25*, 536−541.

(12) Chen, S.; Duan, J.; Han, W.; Qiao, S. Z. *Chem. Commun.* **2014**, *50*, 207−209.

(13) Wei, Z. D.; Huang, W. Z.; Zhang, S. T.; Tan, J. *J. Appl. Electrochem.* **2000**, *30*, 1133−1136.

(14) Mette, K.; Bergmann, A.; Tessonnier, J. P.; Havecker, M.; Yao, L. D.; Ressler, T.; Schlogl, R.; Strasser, P.; Behrens, M. *ChemCatChem* **2012**, *4*, 851−862.

(15) Wei, L.; Li, C. Q.; Chu, H. B.; Li, Y. *Dalton Transactions* **2011**, *40*, 2332−2337.

(16) Tang, Q. E.; Jiang, L. H.; Qi, J.; Jiang, Q.; Wang, S. L.; Sun, G. Q. *Appl. Catal., B* **2011**, *104*, 337−345.

(17) Sun, W.; Hsu, A.; Chen, R. R. *J. Power Sources* **2011**, *196*, 4491−4498.

(18) Tang, Q.; Jiang, L.; Qi, J.; Jiang, Q.; Wang, S. L.; Sun, G. Q. *Appl. Catal., B* **2011**, *104*, 337−345.

(19) Garcia, A. C.; Herrera, A. D.; Ticianelli, E. A.; Chatenet, M.; Poinsignon, C. *J. Electrochem. Soc.* **2011**, *158*, B290−B296.

(20) Wang, X.; Li, Y. D. *J. Am. Chem. Soc.* **2002**, *124*, 2880−2881.

(21) Omomo, Y.; Sasaki, T.; Wang, L. Z.; Watanabe, M. *J. Am. Chem. Soc.* **2003**, *125*, 3568−3575.

(22) Jafri, R. I.; Sujatha, N.; Rajalakshmi, N.; Ramaprabhu, S. *Int. J. Hydrogen Energy* **2009**, *34*, 6371−6376.

(23) Cao, Y. L.; Yang, H. X.; Ai, X. P.; Xiao, L. F. *J. Electroanal. Chem.* **2003**, *557*, 127−134.

(24) Cheng, F.; Su, Y.; Liang, J.; Tao, Z.; Chen, J. *Chem. Mater.* **2010**, *22*, 898−905.

(25) Xiao, W.; Wang, D.; Lou, X. W. *J. Phys. Chem. C* **2010**, *114*, 1694−1700.

(26) Mao, L.; Zhang, D.; Sotomura, T.; Nakatsu, K.; Koshiba, N.; Ohsaka, T. *Electrochim. Acta* **2003**, *48*, 1015−1021.

(27) Cheng, F.; Shen, J.; Ji, W.; Tao, Z.; Chen, J. *ACS Appl. Mater. Interfaces* **2009**, *1*, 460−466.

(28) Lv, Y.; Liu, Y.; Zhu, Y.; Zhu, Y. *J. Mater. Chem. A* **2014**, *2*, 1174−1182.

(29) Lim, W. F.; Cheong, K. Y. *Phys. Chem. Chem. Phys.* **2014**, *16*, 7015−7022.

(30) Zhou, H.; Shi, Y.; Wang, L.; Zhang, H.; Zhao, C.; Hagfeldt, A.; Ma, T. *Chem. Commun. (Cambridge, U. K.)* **2013**, *49*, 7626−7628.

(31) Negreira, A. S.; Aboud, S.; Wilcox, J. *Phys. Rev. B: Condens. Matter Mater. Phys.* **2011**, *83*, 045423−1−14.

(32) Li, J. B.; Jiang, Z. Q.; Qian, K.; Huang, W. X. *Chin. J. Chem. Phys.* **2012**, *25*, 103−109.

(33) Zhao, H.; Wang, J.; Zhang, L.; Rong, Y.; Chen, J.; Ibrahim, K.; Xing, X. *Dalton Trans* **2013**, *42*, 10358−10364.

(34) Kong, M.; Li, Y.; Chen, X.; Tian, T.; Fang, P.; Zheng, F.; Zhao, X. *J. Am. Chem. Soc.* **2011**, *133*, 16414−16417.

(35) Yan, J.; Wu, G.; Guan, N.; Li, L.; Li, Z.; Cao, X. *Phys. Chem. Chem. Phys.* **2013**, *15*, 10978−10988.

(36) Sun, C. H.; Wang, Y.; Zou, J.; Smith, S. C. *Phys. Chem. Chem. Phys.* **2011**, *13*, 11325−11328.

(37) Oxford, G. A. E.; Chaka, A. M. *J. Phys. Chem. C* **2011**, *115*, 16992−17008.

(38) Lima, F. H. B.; Calegaro, M. L.; Ticianelli, E. A. *Electrochim. Acta* **2007**, *52*, 3732−3738.

(39) Roche, I.; Chainet, E.; Vondrak, J.; Chatenet, M. *J. Appl. Electrochem.* **2008**, *38*, 1195−1201.

(40) Ananth, M. V.; Giridhar, V. V.; Renuga, K. *Int. J. Hydrogen Energy* **2009**, *34*, 658−664.

(41) Kalubarme, R. S.; Cho, M. S.; Yun, K. S.; Kim, T. S.; Park, C. J. *Nanotechnology* **2011**, *22*, 395402.

(42) Lima, F. H. B.; Calegaro, M. L.; Ticianelli, E. A. *Electrochim. Acta* **2007**, *52*, 3732−3738.

(43) Roche, I.; Chainet, E.; Chatenet, M.; Vondrak, J. *J. Phys. Chem. C* **2007**, *111*, 1434−1443.

(44) Calegaro, M. L.; Lima, F. H. B.; Ticianelli, E. A. *J. Power Sources* **2006**, *158*, 735−739.

(45) Zhang, W. X.; Wang, H.; Yang, Z. H.; Wang, F. *Colloids Surf., A* **2007**, *304*, 60−66.

(46) Valim, R. B.; Santos, M. C.; Lanza, M. R. V.; Machado, S. A. S.; Lima, F. H. B.; Calegaro, M. L. *Electrochim. Acta* **2012**, *85*, 423−431.

(47) Vondrák, J.; Klápšť, B.; Velická, J.; Sedlaříková, M.; Reiter, J.; Roche, I.; Chainet, E.; Fauvarque, J. F.; Chatenet, M. *J. New Mater. Electrochem. Syst.* **2005**, *8*, 209−212.

(48) Wei, Z. D.; Huang, W. Z.; Zhang, S. T.; Tan, J. *J. Power Sources* **2000**, *91*, 83−85.

(49) Krcha, M. D.; Janik, M. J. *Langmuir* **2013**, *29*, 10120−10131.

(50) Oxford, G. A. E.; Chaka, A. M. *J. Phys. Chem. C* **2012**, *116*, 11589−11605.

(51) Ruetschi, P.; Giovanoli, R. *J. Appl. Electrochem.* **1982**, *12*, 109−114.

(52) Greiner, M. T.; Chai, L.; Helander, M. G.; Tang, W.-M.; Lu, Z.-H. *Adv. Funct. Mater.* **2012**, *22*, 4557−4568.

(53) Fareid ul Islam, A. K. M.; Islam, R.; Khan, K. A. *J. Mater. Sci.: Mater. Electron.* **2005**, *16*, 203−207.

(54) Li, L.; Wei, Z.; Chen, S.; Qi, X.; Ding, W.; Xia, M.; Li, R.; Xiong, K.; Deng, Z.; Gao, Y. *Chem. Phys. Lett.* **2012**, *539−540*, 89−93.

(55) Tang, Q. W.; Jiang, L. H.; Liu, J.; Wang, S. L.; Sun, G. Q. *ACS Catal.* **2014**, *4*, 457−463.